ORIGINAL PAPER

On the effects of rotor induced vibrational stability on helicopter flight dynamics

Umberto Saetti[1] · Joseph F. Horn[2] · Tom Berger[3]

Abstract

This article investigates vibrational stabilization effects in rotorcraft flight dynamics. This study is motivated by recent results in flapping-wing flight, which showed that the time-varying aerodynamic and inertial loads due to the insect wing periodic motion induce a vibrational stabilization mechanism in hover. The dynamics of flapping-wing flyers and rotary-wing vehicles are both described by time-periodic systems so vibrational stabilization mechanisms can also have an effect on stability characteristics of rotary-wing vehicles. The article extends the use of the harmonic decomposition method to vibrational stability analysis of rotorcraft. Two cases are considered: vibrational stability due blade imbalance at hover, and vibrational stability due to number-of-blades-per-rotor-revolution (N_b/rev) in high-speed forward flight. Results show that while vibrations induced by rotor blade imbalance do not stabilize the hovering dynamics of a helicopter, these vibrations can still have a significant effect on the hovering dynamics. Rotor blade imbalance results in a symmetric effect on the roll and pitch axes, in that it tends to decrease the frequency of the subsidence modes of the hovering cubic, while the unstable oscillatory modes tend to increase in frequency and decrease in damping (destabilizing effect). On the other hand, the yaw/heave dynamics are relatively unaffected compared to the lateral and longitudinal axes. Moreover, N_b/rev rotor loads in forward flight are shown to reduce the damping of the coupled roll/pitch oscillation mode.

Keywords Rotorcraft · Flight dynamics and control · Time-periodic systems · System identification

1 Introduction

Vibrational stabilization is a phenomena where the unstable dynamics of a system about an equilibrium point of interest can be stabilized via periodic forcing of the system at a high-enough forcing frequency [1, 2]. Examples of this phenomena include, but are not limited to, those involving an inverted pendulum with vibrating suspension point [3]

✉ Umberto Saetti
saetti@umd.edu

Joseph F. Horn
joehorn@psu.edu

Tom Berger
tom.berger2.civ@army.mil

[1] Department of Aerospace Engineering, University of Maryland, College Park, MD 20742, USA

[2] Department of Aerospace Engineering, The Pennsylvania State University, University Park, PA 16802, USA

[3] U.S. Army Combat Capabilities Development, Command Aviation and Missile, Moffett Field 94035, CA, USA

and hovering insects where their hovering cubic [4] is stabilized by the wing periodic flapping motion [5, 6]. In the latter case, the wing flapping motion inducing a vibrational stabilization mechanism that increases the pitch damping and stiffness while reducing the speed stability. This results in stabilization of the pitch oscillatory mode and thus of the longitudinal hovering cubic.

Despite apparent differences in shape and dimension, the dynamics of flapping-wing flyers are indeed mathematically similar to those of rotary-wing vehicles such as helicopters. This stems from the time-varying aerodynamic and inertial loads due to the wing/blade periodic motion. In fact, the dynamics of both flapping- and rotary-wing flight are described by nonlinear time-periodic (NLTP) systems of the coupled rigid-body and complex interactional aerodynamics between the wings/blades, body, and the self-induced wake. However, the relative importance of the time-periodic dynamics (i.e., those dynamics with natural frequencies that are multiples of the fundamental frequency of the system) and the overall dynamics of the system (i.e., averaged + time-periodic dynamics) are significantly higher for flapping-wing flyers than

they are for helicopters—approximately 7% for helicopters [7] and up to 50% for flapping-wing flyers [8, 9]. These estimates were obtained using modal participation factors [10]. In light of these similarities, this study was carried out to see if the virbrational stabilization mechanisms that are observed for flapping-wing flight also extend to rotary-wing flight.

One major challenge in the analysis of vibrational stabilization lies in the stability analysis of NLTP systems. While the stability analysis of nonlinear time-invariant (NLTI) systems is readily assessed by linearizing the dynamics about an equilibrium point and performing eigenanalysis, or by means of Lyapunov theory, the stability analysis of NLTP systems is typically a more challenging task. This is because the equilibrium solution of NLTP systems is typically represented by a periodic orbit rather than by a fixed point. Three main approaches exist for determining the stability of NLTP systems (Fig. 1) [11, 12]: the first is based on Floquet theory [13–17], the second is based on averaging methods [11, 18–26], and the third is based on Lyapunov characteristic exponents (LCE) [12, 27–32]. The first approach is articulated in the following four major steps: (1) a periodic orbit is found by solving the dynamic equations, (2) the dynamic equations are linearized about that periodic orbit to yield a linear time-periodic (LTP) system, (3) the LTP system is transformed into a linear time-invariant (LTI) system via Floquet transformation/decomposition, and (4) stability is assessed by checking the eigenvalues of the LTI system. The second approach to determine stability of NLTP systems leverages averaging methods to transform the NLTP system into an equivalent NLTI system where the periodic orbit of the original system collapses to a single point in the state space. Stability is thus assessed by linearizing the equivalent NLTI system about its equilibrium point and by performing spectral analysis [18]. The third method generalizes the stability solutions of the linear models, i.e., eigenvalues of LTI systems and Floquet multipliers of linear time-periodic (LTP) systems, to the case of non-linear, time-varying systems. LCE are directly computed from the non-linear, time-varying dynamics and avoid the linearization step.

Historically, the only methods available for transforming the LTP dynamics into approximate higher-order LTI systems were the Lyapunov-Floquet method [33] and frequency lifting methods [34], which both suffered from the common disadvantage of the need for state transition matrices. State transition matrices constitute a particular challenge in that their computation can be numerically intensive and/or very sensitive to tuning parameters which require prior knowledge on the system's dynamics. However, this limitation can be relaxed using the *harmonic decomposition* method that originated from the rotorcraft community [35–37]. Within the context of rotorcraft, harmonic decomposition models have been used to: (1) study the interference effects between higher-harmonic control (HHC) and the aircraft flight control system (AFCS) [35, 38–40]; (2) design load alleviation control (LAC) laws (the PI's efforts in [41–43]; and (3) prediction and avoidance of flight envelope limits [43–45]. A survey by the PI on the use of harmonic decomposition models in the rotorcraft field can be found in [46]. When coupled with a harmonic balance scheme, harmonic decomposition can also be used to solve for (stable and unstable) periodic solutions [47] and compute open-loop higher-harmonic control (HHC) inputs that attenuate arbitrary state/output harmonics [9]. Because harmonic decomposition (1) relaxes all limitations associated with the Floquet-based approach and (2) can be used to compute unstable periodic orbits (note that the unaugmented hover dynamics of rotorcraft is unstable, see [4], it is used to analyze vibrational stability of rotorcraft in this study.

The objective of this article is to investigate vibrational stability effects in rotorcraft flight dynamics. To do so, the harmonic decomposition method is extended to the vibrational stability analysis of rotorcraft and used to assess: (1) the effect of blade imbalance—one-per-rotor-revolution (1/rev) vibrations—on the hover flight dynamics of a conventional utility helicopter similar to a UH-60 and (2) the effect of number-of-blades per rotor revolution (N_b/rev) vibrations in high-speed forward flight on the flight dynamics of the same helicopter model. The specific contributions of this article are: (1) the extension of the harmonic decomposition method for the study of rotorcraft vibrational stability, and (2) the investigation of vibrational stability effects in rotorcraft flight dynamics for the specific cases of rotor blade imbalance at hover and N_b/rev loads in high-speed forward flight.
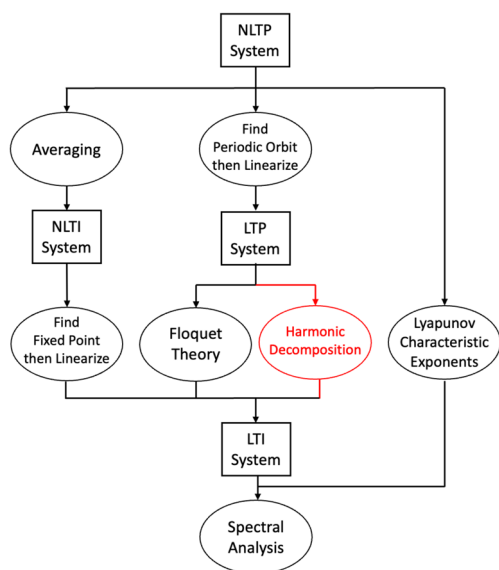
Fig. 1 Illustration of the three main approaches to stability analysis of NLTP systems: averaging methods (left), Floquet theory and harmonic decomposition (center), and Lyapunov characteristic exponents (right)

The article starts from a simple example involving an inverted pendulum to demonstrate the use of the harmonic decomposition method [35, 36] for the study of vibrational stabilization effects. The concept is then extended to analyze the effect of blade imbalance on the flight dynamics of a hovering helicopter, as well as the effect of N_b/rev loads in high-speed forward flight. Final remarks summarize the overall findings of the study and future developments are identified.

2 Mathematical background

2.1 Harmonic decomposition

Consider a nonlinear time-periodic (NLTP) system in first-order form representative of the rotorcraft flight dynamics:

$$\dot{x} = f(x, u, t) \tag{1a}$$

$$y = g(x, u, t) \tag{1b}$$

where $x \in \mathbb{R}^n$ is the state vector, $u \in \mathbb{R}^m$ is the control input vector, $y \in \mathbb{R}^l$ is the output vector, and t is the dimensional time in seconds. The nonlinear functions f and g are T-periodic in time such that:

$$f(x, u, t) = f(x, u, t + T) \tag{2a}$$

$$g(x, u, t) = g(x, u, t + T) \tag{2b}$$

Note that the fundamental period of the system is $T = \frac{2\pi}{\Omega}$ seconds, where Ω is the angular speed of the main rotor in rad/s. Let $x^*(t)$ and $u^*(t)$ represent a periodic solution of the system such that $x^*(t) = x^*(t + T)$ and $u^*(t) = u^*(t + T)$. Then, the NLTP system can be linearized about the periodic solution. Linearized time-invariant/periodic approximations are typically considered acceptable in rotorcraft flight dynamics, especially to assess dynamic stability and response characteristics about an equilibrium (or trim) condition. Should the NLTP dynamics deviate significantly from the trim condition, then linearized approximations would no longer be accurate. Consider the case of small disturbances:

$$x = x^* + \Delta x \tag{3a}$$

$$u = u^* + \Delta u \tag{3b}$$

where Δx and Δu are the state and control perturbation vectors from the candidate periodic solution. A Taylor series expansion is performed on the state derivative and output vectors. Neglecting terms higher than first order results in the following equations:

$$f(x^* + \Delta x, u^* + \Delta u, t) = f(x^*, u^*, t) + F(t)\Delta x + G(t)\Delta u \tag{4a}$$

$$g(x^* + \Delta x, u^* + \Delta u, t) = g(x^*, u^*, t) + P(t)\Delta x + Q(t)\Delta u \tag{4b}$$

where:

$$F(t) = \left.\frac{\partial f(x, u)}{\partial x}\right|_{x^*, u^*}, \tag{5a}$$

$$G(t) = \left.\frac{\partial f(x, u)}{\partial u}\right|_{x^*, u^*} \tag{5b}$$

$$P(t) = \left.\frac{\partial g(x, u)}{\partial x}\right|_{x^*, u^*}, \tag{5c}$$

$$Q(t) = \left.\frac{\partial g(x, u)}{\partial u}\right|_{x^*, u^*} \tag{5d}$$

Note that the state-space matrices in Eq. (5) have T-periodic coefficients such that:

$$F(t) = F(t + T), \tag{6a}$$

$$G(t) = G(t + T) \tag{6b}$$

$$P(t) = P(t + T), \tag{6c}$$

$$Q(t) = Q(t + T) \tag{6d}$$

Equations (4a) and (4b) yield a linear time-periodic (LTP) approximation of the NLTP system of Eq. (1) as follows:

$$\Delta\dot{x} = F(t)\Delta x + G(t)\Delta u \tag{7a}$$

$$\Delta y = P(t)\Delta x + Q(t)\Delta u \tag{7b}$$

Hereafter, the notation is simplified by dropping the Δ in front of the linearized perturbation state and control vectors while keeping in mind that these vectors represent perturbations from a periodic equilibrium. Next, the state, input, and output vectors of the LTP systems are decomposed into a finite number of harmonics of the fundamental period via Fourier analysis:

$$x = x_0 + \sum_{i=1}^{N} x_{ic} \cos\left(\frac{2\pi i t}{T}\right) + x_{is} \sin\left(\frac{2\pi i t}{T}\right) \tag{8a}$$

$$u = u_0 + \sum_{j=1}^{M} u_{jc} \cos\left(\frac{2\pi j t}{T}\right) + u_{js} \sin\left(\frac{2\pi j t}{T}\right) \tag{8b}$$

$$y = y_0 + \sum_{k=1}^{L} y_{kc} \cos\left(\frac{2\pi k t}{T}\right) + y_{ks} \sin\left(\frac{2\pi k t}{T}\right) \quad (8c)$$

As shown in [35], the harmonic decomposition methodology can be used to transform the LTP model into an approximate higher-order linear time-invariant (LTI) model in first-order form:

$$\dot{X} = AX + BU \quad (9a)$$

$$Y = CX + DU \quad (9b)$$

where the augmented state, control, and output vectors $X \in \mathbb{R}^{n(2N+1)}$, $U \in \mathbb{R}^{m(2M+1)}$, and $Y \in \mathbb{R}^{l(2L+1)}$, respectively, are given by:

$$X^T = \begin{bmatrix} x_0^T & x_{1c}^T & x_{1s}^T & \cdots & x_{Nc}^T & x_{Ns}^T \end{bmatrix} \quad (10a)$$

$$U^T = \begin{bmatrix} u_0^T & u_{1c}^T & u_{1s}^T & \cdots & u_{Mc}^T & u_{Ms}^T \end{bmatrix} \quad (10b)$$

$$Y^T = \begin{bmatrix} y_0^T & y_{1c}^T & y_{1s}^T & \cdots & y_{Lc}^T & y_{Ls}^T \end{bmatrix} \quad (10c)$$

with $A \in \mathbb{R}^{n(2N+1) \times n(2N+1)}$, $B \in \mathbb{R}^{n(2N+1) \times m(2M+1)}$, $C \in \mathbb{R}^{l(2L+1) \times n(2N+1)}$, and $D \in \mathbb{R}^{l(2L+1) \times m(2M+1)}$. Closed-form expressions for these matrices can be found in [35]. It is worth noting that harmonic decomposition does not rely on state transition matrices, which makes the methodology more computationally efficient and less numerically sensitive than other approaches such as the Lyapunov-Floquet method [33] and frequency lifting methods [34].

2.2 Model-order reduction

Because one of the objectives of this article is to investigate the change in stability derivatives that results from vibrational stabilization, it is desired to reduce the order of the harmonic decomposition models down to a model that is representative of rigid-body dynamics. Ideally, these reduced-order models do not include the higher harmonic states but still retain part of the higher-harmonic response characteristics. This can be achieved through residualization, a portion of singular perturbation theory that pertains to LTI systems [48]. Assuming that one or more states of the system have stable dynamics which are faster than that of the remaining states, the state vector in Eq. (10a) can be partitioned into fast X_f and slow X_s components:

$$X^T = \begin{bmatrix} X_s^T & X_f^T \end{bmatrix} \quad (11)$$

Then, the system in Eq. (9a) can be re-written as:

$$\begin{bmatrix} \dot{X}_s \\ \dot{X}_f \end{bmatrix} = \begin{bmatrix} A_s & A_{sf} \\ A_{fs} & A_f \end{bmatrix} \begin{bmatrix} X_s \\ X_f \end{bmatrix} + \begin{bmatrix} B_s \\ B_f \end{bmatrix} U \quad (12)$$

By assuming that the dynamics of the fast states reach steady-state in the time scale of interest (i.e., $\dot{X}_f = 0$) and performing a few algebraic manipulations, the equations for a reduced-order system with the state vector composed of the slow states may be found:

$$\dot{X}_s = \hat{A}X_s + \hat{B}U \quad (13)$$

where:

$$\hat{A} = A_s - A_{sf}A_f^{-1}A_{fs} \quad (14a)$$

$$\hat{B} = B_s - A_{sf}A_f^{-1}B_f \quad (14b)$$

Note that A_f must be invertible. This is guaranteed if A_f is non-singular, i.e., no eigenvalue has a real-part that is equal to zero. Additionally, to apply residualization, A_f must be is asymptotically stable, i.e., all eigenvalues have their real part that is strictly negative. In this study, the slow states are chosen as the zeroth harmonic rigid-body states with the exception of the position states as the flight dynamics are invariant with respect to these [49], whereas the fast states are taken as the higher harmonics of the rotor states [9, 42, 50, 51]:

$$X_s^T = \begin{bmatrix} u_0 & v_0 & w_0 & p_0 & q_0 & r_0 & \phi_0 & \theta_0 & \psi_0 \end{bmatrix} \quad (15a)$$

$$X_f^T = \begin{bmatrix} x_{R_0}^T & x_{R_{1c}}^T & \cdots & x_{R_{Ns}}^T \end{bmatrix} \quad (15b)$$

In the equation above,

u, v, w are the longitudinal, lateral, and vertical velocities in the body-fixed frame,
p, q, r are the roll, pitch, and yaw rates,
ϕ, θ, ψ are the Euler angles,
x, y, z are the positions in the North-East-Down (NED) frame,

whereas x_R are the rotor states. More detail on the rotor states is provided later in this article. The rotor states are generally asymptotically stable, unless there is some aero-mechanic/aeroelastic instability, which is not modelled herein. This guarantees A_f to be asymptotically stable. Note that the higher harmonics of the rigid-body states were truncated from the fast state vector. This is because the higher harmonics of the rigid-body states are generally unstable at hover and low-to-moderate speeds (their eigenvalues are shifted on the imaginary axis with respect to the zeroth-harmonic eigenvalues by $k\Omega$, with $k = 1, \ldots, N$). This would cause A_f not to be asymptotically stable. The truncation of these states is justified by the fact that the higher harmonics of the rigid body states have negligible contribution to the overall flight dynamics [7]. An alternative reduction that

yields a 10-state model involves retaining the longitudinal and lateral flapping angles as part of the slow state vector [42], such that:

$$\boldsymbol{X}_s^T = \begin{bmatrix} u_0 \, v_0 \, w_0 \, p_0 \, q_0 \, r_0 \, \phi_0 \, \theta_0 \, \psi_0 \, \beta_{1c} \, \beta_{1s} \end{bmatrix} \quad (16a)$$

$$\boldsymbol{X}_f^T = \begin{bmatrix} \hat{\boldsymbol{x}}_{R_0}^T \, \boldsymbol{x}_{R_{1c}}^T \, \cdots \, \boldsymbol{x}_{R_{Ns}}^T \end{bmatrix} \quad (16b)$$

where $\hat{\boldsymbol{x}}_{R_0}$ is the zeroth harmonic of the rotor state vector with the longitudinal and lateral flapping states removed, and β_{1c} and β_{1s} are the longitudinal and lateral flapping angles, respectively. The 10-state model will model the regressive flap mode and be accurate, at least for the UH-60 helicopter, up to about 10 rad/s, compared to approximately the 4 rad/s of the 8-state model retaining the rigid-body dynamics only [52, 53]. It is worth mentioning that the regressive flap mode has a natural frequency that is significantly less than the slowest first harmonic component of the flight dynamics. In fact, harmonic components are at frequencies multiple of the fundamental frequency of the system, i.e., 27 rad/s for the UH-60. The minimum-frequency first harmonic components will be at 27 rad/s. Thus, the frequency separation between the fastest "slow" state and the slowest "fast" state is significant such that residualization is justified. Both methods are used in this article.

To ensure the residualized model retains information about the influence of the residualized dynamics on both the zeroth harmonics and the higher output harmonics of the output, consider partitioning the output equations in Eq. (9b) as:

$$\boldsymbol{Y} = \begin{bmatrix} \boldsymbol{C}_s \, \boldsymbol{C}_f \end{bmatrix} \begin{bmatrix} \boldsymbol{X}_s \\ \boldsymbol{X}_f \end{bmatrix} + \boldsymbol{DU} \quad (17)$$

Then, it can be shown that the residualized output equations are:

$$\dot{\boldsymbol{Y}} = \hat{\boldsymbol{C}} \boldsymbol{X}_s + \hat{\boldsymbol{D}} \boldsymbol{U} \quad (18)$$

where:

$$\hat{\boldsymbol{C}} = \boldsymbol{C}_s - \boldsymbol{C}_f \boldsymbol{A}_f^{-1} \boldsymbol{A}_{fs} \quad (19a)$$

$$\hat{\boldsymbol{D}} = \boldsymbol{D} - \boldsymbol{C}_f \boldsymbol{A}_f^{-1} \boldsymbol{B}_f \quad (19b)$$

If now the augmented output vector is selected to coincide with the harmonics of the output vector in Eq. (20), such that:

$$\boldsymbol{Y}^T = \begin{bmatrix} \boldsymbol{y}_0^T \, \boldsymbol{y}_{1c}^T \, \boldsymbol{y}_{1s}^T \, \cdots \, \boldsymbol{y}_{Lc}^T \, \boldsymbol{y}_{Ls}^T \end{bmatrix} \quad (20)$$

then, the residualized model will predict the influence of the residualized dynamics on the zeroth and higher-harmonic of the output.

3 Vibrational stability

3.1 Inverted pendulum dynamics

The overall methodology used for this investigation, i.e., the use of harmonic decomposition to assess vibrational stability, is explained through a simple example involving an inverted pendulum [3, 54] with a vibrating suspension point, shown in Fig. 2. Consider the dynamics of such pendulum:

$$L\ddot{\theta} - (g + A)\theta = 0 \quad (21)$$

where L is the pendulum length, A the acceleration resulting from the periodic displacement of the point of suspension, and g is the gravitational acceleration.

Assume that the displacement of the point of suspension is given by:

$$D = a \sin \psi \quad (22)$$

where $\psi = \Omega t$. Then, the acceleration A of the suspension point is:

$$A = \ddot{D} = -a\Omega^2 \sin \psi \quad (23)$$

The system in Eq. (21) can be reformulated as a system of ordinary differential equations (ODEs) such that:
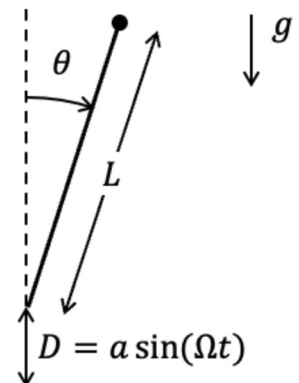
$$\dot{\boldsymbol{x}} = \begin{bmatrix} 0 & \frac{g}{L} - \frac{a}{L}\Omega^2 \sin \psi \\ 1 & 0 \end{bmatrix} \boldsymbol{x} = \boldsymbol{F}(\psi)\boldsymbol{x} \quad (24)$$

where $\boldsymbol{x}^T = \begin{bmatrix} \dot{\theta} \, \theta \end{bmatrix}$. Note that $\boldsymbol{F}(\psi) = \boldsymbol{F}(\psi + \Omega T)$, where $T = 2\pi/\Omega$. Thus, the system in Eq. (24) is a linear time-periodic (LTP) system.

3.2 Harmonic decomposition models

Consider now decomposing the state vector into harmonics of the fundamental frequency Ω, such that:

Fig. 2 Inverted pendulum with the point of suspension being vibrated

$$x = x_0 + \sum_{n=1}^{N} \left[x_{nc} \cos(n\psi) + x_{ns} \sin(n\psi) \right] \tag{25}$$

Then, it can be shown [35, 36] that the system in Eq. (24) is approximated with a higher-order linear time-invariant (LTI) system of the form:

$$A = \begin{bmatrix} H_{0F} & H_{0F^{1c}} & H_{0F^{1s}} & \cdots & H_{0F^{Nc}} & H_{0F^{Ns}} \\ H_{1cF} & H_{1cF^{1s}} & -\Omega + H_{1cF^{1s}} & \cdots & H_{1cF^{Nc}} & H_{1cF^{Ns}} \\ H_{1sF} & \Omega + H_{1sF^{1s}} & H_{1sF^{1s}} & \cdots & H_{1sF^{Nc}} & H_{1sF^{Ns}} \\ \vdots & \vdots & \vdots & \ddots & \vdots & \vdots \\ H_{NcF} & H_{NcF^{1s}} & H_{NcF^{1s}} & \cdots & H_{NcF^{Nc}} & -N\Omega + H_{NcF^{Ns}} \\ H_{NsF} & H_{NsF^{1s}} & H_{NsF^{1s}} & \cdots & N\Omega + H_{NsF^{Nc}} & H_{NsF^{Ns}} \end{bmatrix} \tag{26}$$

The A matrix coefficients are given by:

$$H_{0F} = \frac{1}{2\pi} \int_0^{2\pi} F(\psi) d\psi \tag{27a}$$

$$H_{icF} = \frac{1}{\pi} \int_0^{2\pi} F(\psi) \cos(i\psi) d\psi \tag{27b}$$

$$H_{isF} = \frac{1}{\pi} \int_0^{2\pi} F(\psi) \sin(i\psi) d\psi \tag{27ba-c}$$

$$H_{0F^{nc}} = \frac{1}{2\pi} \int_0^{2\pi} F^{nc}(\psi) d\psi \tag{27c}$$

$$H_{icF^{nc}} = \frac{1}{\pi} \int_0^{2\pi} F^{nc}(\psi) \cos(i\psi) d\psi \tag{27d}$$

$$H_{isF^{nc}} = \frac{1}{\pi} \int_0^{2\pi} F^{nc}(\psi) \sin(i\psi) d\psi \tag{27dd-f}$$

$$H_{0F^{ns}} = \frac{1}{2\pi} \int_0^{2\pi} F^{ns}(\psi) d\psi \tag{27e}$$

$$H_{icF^{ns}} = \frac{1}{\pi} \int_0^{2\pi} F^{ns}(\psi) \cos(i\psi) d\psi \tag{27f}$$

$$H_{isF^{ns}} = \frac{1}{\pi} \int_0^{2\pi} F^{ns}(\psi) \sin(i\psi) d\psi \tag{27fg-i}$$

where:

$$F^{nc}(\psi) = F(\psi) \cos(n\psi) \tag{28a}$$

$$F^{ns}(\psi) = F(\psi) \sin(n\psi) \tag{28b}$$

The following example involves retaining up to the first harmonic in the harmonic decomposition of state vector in Eq. (25). By doing so, the LTP system in Eq. (24) is transformed into an equivalent LTI system with a system matrix:

$$A = \begin{bmatrix} 0 & \frac{g}{L} & 0 & 0 & 0 & \Omega^2 \frac{a}{2L} \\ 1 & 0 & 0 & 0 & 0 & 0 \\ 0 & 0 & 0 & \frac{g}{L} & -\Omega & 0 \\ 0 & 0 & 1 & 0 & 0 & -\Omega \\ 0 & \Omega^2 \frac{a}{L} & \Omega & 0 & 0 & \frac{g}{L} \\ 0 & 0 & 0 & \Omega & 1 & 0 \end{bmatrix} \tag{29}$$

and where $x^T = \begin{bmatrix} \dot\theta_0 & \theta_0 & \dot\theta_{1c} & \theta_{1c} & \dot\theta_{1s} & \theta_{1s} \end{bmatrix}$ is the augmented state vector. The stability of the system will be determined by the eigenvalues of the A matrix. The eigenvalues are given by:

$$\lambda_{1,2} = \pm c_1 \tag{30a}$$

$$\lambda_{3,4} = \pm c_2 \tag{30b}$$

$$\lambda_{5,6} = \pm \sqrt{c_3 + c_4 - \frac{c_5}{c_3}} \tag{30c}$$

where:

$$c_1 = \sqrt{c_4 - \frac{c_3}{2} + \frac{c_5}{2c_3} - \frac{1}{2}\sqrt{3}\left(c_3 \frac{c_5}{c_3} i\right)} \tag{31a}$$

$$c_2 = \sqrt{c_4 - \frac{c_3}{2} + \frac{c_5}{2c_3} + \frac{1}{2}\sqrt{3}\left(c_3 \frac{c_5}{c_3} i\right)} \tag{31b}$$

$$c_3 = \left\{ c_6 + \sqrt{\left[c_6 + \frac{\left(6L^2 g - 4L^3 \Omega^2\right)^3}{216 L^9} - c_7 \right]^2 + c_5^3} + \frac{\left(6L^2 g - 4L^3 \Omega^2\right)^3}{216 L^9} - c_7 \right\}^{1/3} \tag{31c}$$

$$c_4 = \frac{6L^2 g - 4L^3 \Omega^2}{6L^3} \tag{31d}$$

$$c_5 = \frac{2L^3 \Omega^4 - L\Omega^4 a^2 + 6Lg^2}{6L^3} - \frac{\left(6L^2 g - 4L^3 \Omega^2\right)^2}{36 L^6} \tag{31e}$$

$$c_6 = \frac{2L^2 \Omega^4 g - L\Omega^6 a^2 + 4L\Omega^2 g^2 - \Omega^4 a^2 g + 2g^3}{4L^3} \tag{31f}$$

$$c_7 = \frac{\left(6L^2 g - 4L^3 \Omega^2\right)\left(2L^3 \Omega^4 - L\Omega^4 a^2 + 6Lg^2\right)}{24 L^6} \tag{31g}$$

It can be shown [3] that the inverted pendulum is stable for a high-enough forcing frequency if:

$$a < \frac{\pi^2}{32}L \tag{32}$$

Consider an inverted pendulum where $g = 9.81\,\text{m/s}^2$, $L = 1$ m, and $a = \frac{1}{2}\left(\frac{\pi^2}{32}L\right)$. Then, this pendulum will be stable for forcing frequencies $\Omega \gtrsim 40.59$ rad/s. For instance, the eigenvalues for the case where $\Omega = 0$ rad/s (i.e., no periodic forcing) are:

$$\lambda_1 = 3.1321 \pm 0i, \quad \lambda_2 = -3.1321 \pm 0i \tag{33}$$

whereas the eigenvalues for the case where $\Omega = 50$ rad/s are:

$$\lambda_{1,2} = 0 \pm 4.5314i, \quad \lambda_{3,4} = 0 \pm 47.4166i, \quad \lambda_{5,6} = 0 \pm 51.9779i \tag{34}$$

3.3 Residualization

The order of the system in Eq. (26) can be reduced by means of residualization. As such, the augmented state vector is partitioned into fast and slow components, such that the slow states are chosen as the zeroth harmonic states, whereas the fast states are taken as the higher harmonics:

$$\boldsymbol{X}_s = \boldsymbol{x}_0 \tag{35a}$$

$$\boldsymbol{X}_f^T = [\boldsymbol{x}_{1c}^T \, \boldsymbol{x}_{1s}^T] \tag{35b}$$

Then, the submatrices of Eq. (12) become:

$$\boldsymbol{A}_s = \begin{bmatrix} 0 & \frac{g}{L} \\ 1 & 0 \end{bmatrix} \tag{36a}$$

$$\boldsymbol{A}_{sf} = \begin{bmatrix} 0 & 0 & 0 & \Omega^2 \frac{a}{2L} \\ 0 & 0 & 0 & 0 \end{bmatrix} \tag{36b}$$

$$\boldsymbol{A}_f = \begin{bmatrix} 0 & \frac{g}{L} & -\Omega & 0 \\ 1 & 0 & 0 & -\Omega \\ \Omega & 0 & 0 & \frac{g}{L} \\ 0 & \Omega & 1 & 0 \end{bmatrix} \tag{36c}$$

$$\boldsymbol{A}_{fs} = \begin{bmatrix} 0 & 0 \\ 0 & 0 \\ 0 & \Omega^2 \frac{a}{L} \\ 0 & 0 \end{bmatrix} \tag{36d}$$

Applying Eq. (14) yields the following residualized dynamics:

$$\hat{\boldsymbol{A}} = \begin{bmatrix} 0 & \frac{g}{L} - \frac{\Omega^4 a^2}{2L(L\Omega^2 + g)} \\ 1 & 0 \end{bmatrix} \tag{37}$$

The eigenvalues of this matrix are:

$$\lambda_{1,2} = \pm \frac{\sqrt{2}\sqrt{-\Omega^4 a^2 + 2L\Omega^2 g + 2g^2}}{2\sqrt{L}\sqrt{L\Omega^2 + g}} \tag{38}$$

Setting $\Re(\lambda_{1,2}) = 0$, solving for Ω, and discarding any non-physical solution yields:

$$\Omega = \pm \frac{1}{a}\sqrt{Lg + \sqrt{L^2 g^2 + 2a^2 g^2 + a^2}} \tag{39}$$

$$\approx 28.89\,\text{rad/s}$$

Note that this is only an approximation to the minimum frequency that yields neutral stability.

3.4 Stability maps

To assess the impact of the choice of number of harmonics and of the corresponding residualization on the accuracy of the reduced-order models to describe vibrational stabilization, one can resort to stability maps. Stability maps indicate the regions of stability/instability for varying forcing frequency and amplitude. Stability maps are well known for the inverted pendulum example in consideration. To obtain stability maps, it is convenient to transform the inverted pendulum dynamics into the Mathieu's form [55, 56]:

$$\theta'' + [\alpha + \beta \phi(\tau)]\theta = 0 \tag{40}$$

where $\tau = \psi$ and $\phi(\tau) = \sin \psi$ is the forcing function. Note that:

$$\dot{\theta} = \frac{d\theta}{dt} = \frac{d\theta}{d\tau}\frac{d\tau}{dt} = \theta' \Omega \tag{41a}$$

$$\ddot{\theta} = \frac{d^2\theta}{dt^2} = \frac{d^2\theta}{d\tau^2}\left(\frac{d\tau}{dt}\right)^2 = \theta'' \Omega^2 \tag{41b}$$

By setting Eq. (40) equal to Eq. (21), the following identities are obtained:

$$\alpha = -\frac{g}{L\Omega^2} \tag{42a}$$

$$\beta = \frac{a}{L} \tag{42b}$$

Thus, stability maps can be obtained for varying α and β (Fig. 3). Figure 3a shows the stability map (Ince-Strutt diagram) predicted with the higher-order LTI model derived analytically in the previous section (with $N = 1$), whereas 3b shows the stability map predicted with the

corresponding residualized model. The stability map from the high-order LTI model is somewhat similar to that in [55] for $\beta = a/L < 1$, but differs substantially for $\beta = a/L > 1$. As shown below, this is related to not enough harmonics being retained in the harmonic decomposition process. Compared to the higher-order LTI model, the residualized model is shown to predict the same stability properties for $\alpha \geq 1$. The residualized model also predicts the unstable region for $\alpha < 0$. On the other hand, the prediction $0 \leq \alpha < 1$ is off for values of $\beta > 0$. Nonetheless, the residualized models appears to provide reasonable stability predictions for $\beta = a/L \ll 1$, i.e., at low forcing amplitudes.

Because in Eq. (24) the periodicity is limited to frequencies of one per forcing cycle, one would think it is sufficient to retain up to the first harmonic in the harmonic

decomposition of state vector in Eq. (25). However, as pointed out in [53], harmonics up to one more that of the periodicity must be retained to capture all of the harmonic behaviour. Because of the complexity introduced by the extra harmonics in the calculations compared to the previous case, the high-order LTI model as well as its eigenvalues are computed numerically rather than analytically. Stability maps obtained via harmonic decomposition and corresponding residualized model are shown in Fig. 4 for $N = 2$ state harmonics retained in the harmonic decomposition process. Figure 4a shows stability maps obtained for $N = 2$ whereas 4b shows the corresponding residualized dynamics. In these figures, it is shown how a connection exists between the order of the LTI approximation and the number and shape of parametric resonance or vibrational control regions that

(a) Harmonic decomposition model.

(b) Residualized dynamics.

(c) Comparison between harmonic decomposition and residualized models.
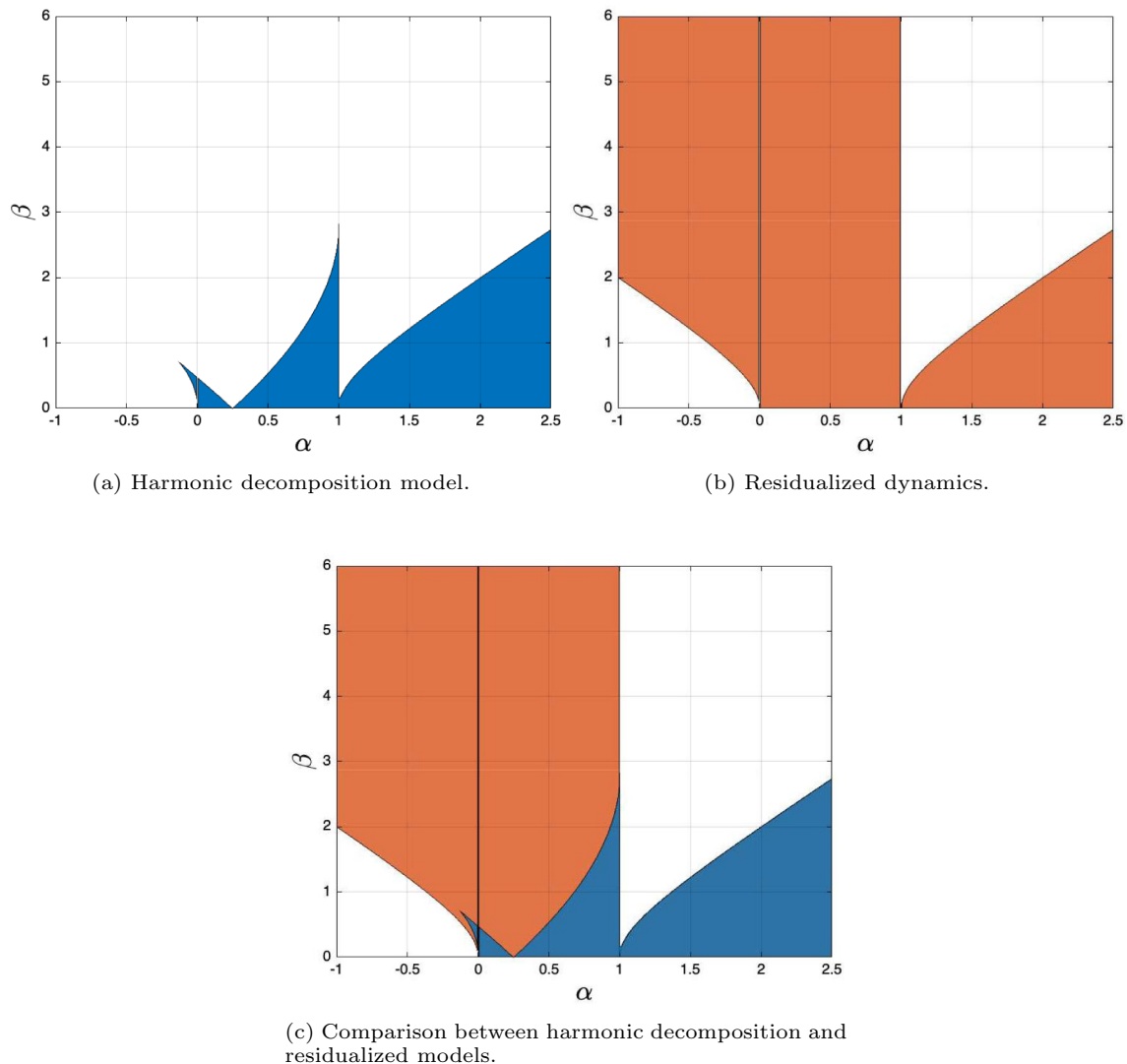
Fig. 3 Stability maps for varying α and β and a sinusoidal forcing function obtained by retaining up to the first state harmonic when performing harmonic decomposition (i.e., $N = 1$)

can be recovered. For $N = 2$, the stability maps from the harmonic decomposition model are identical to those in [55]. The stability map from the residualized model, on the other hand, seems to only predict the left boundaries of the stable regions.

3.5 Time-domain validation

To validate the stability map results obtained with the harmonic decomposition models and corresponding residualized dynamics, time-domain simulations are performed for three cases. These cases, shown via the markers in Fig. 5, correspond to the following $\{\alpha, \beta\}$ combinations:

$\{-0.2, 0.66\}$, $\{-0.2, 0.73\}$, and $\{-0.2, 0.83\}$. Time responses to initial conditions are shown in Fig. 6 for the Mathiew equation, the harmonic decomposition model with $N = 2$, and the corresponding residualized model. Figure 6a, corresponding to $\alpha = -0.2$ and $\beta = 0.66$, shows unstable responses for all of the models. This agrees with the predictions from the stability maps in Fig. 5 and provide a better condition for vibrational stability than averaging methods [54]. Figure 6b, corresponding to $\alpha = -0.2$ and $\beta = 0.73$, shows stable responses for all of the models. This, again, is in line with the prediction provided by the stability map in Fig. 5. However, the response of the residualized model differs from those of the of Mathieu's equation and of the

(a) Harmonic decomposition model.

(b) Residualized dynamics.

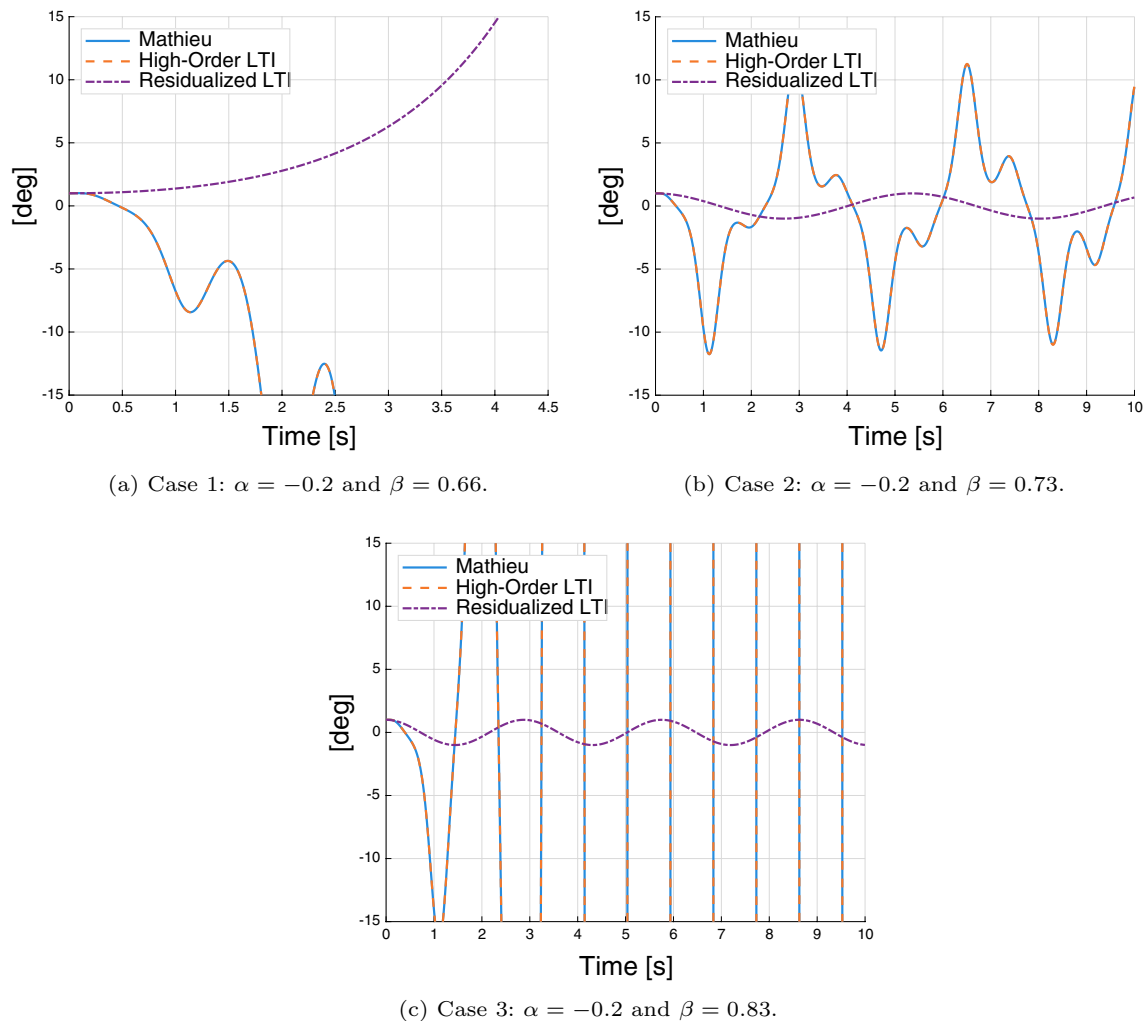(c) Comparison between harmonic decomposition and residualized models.
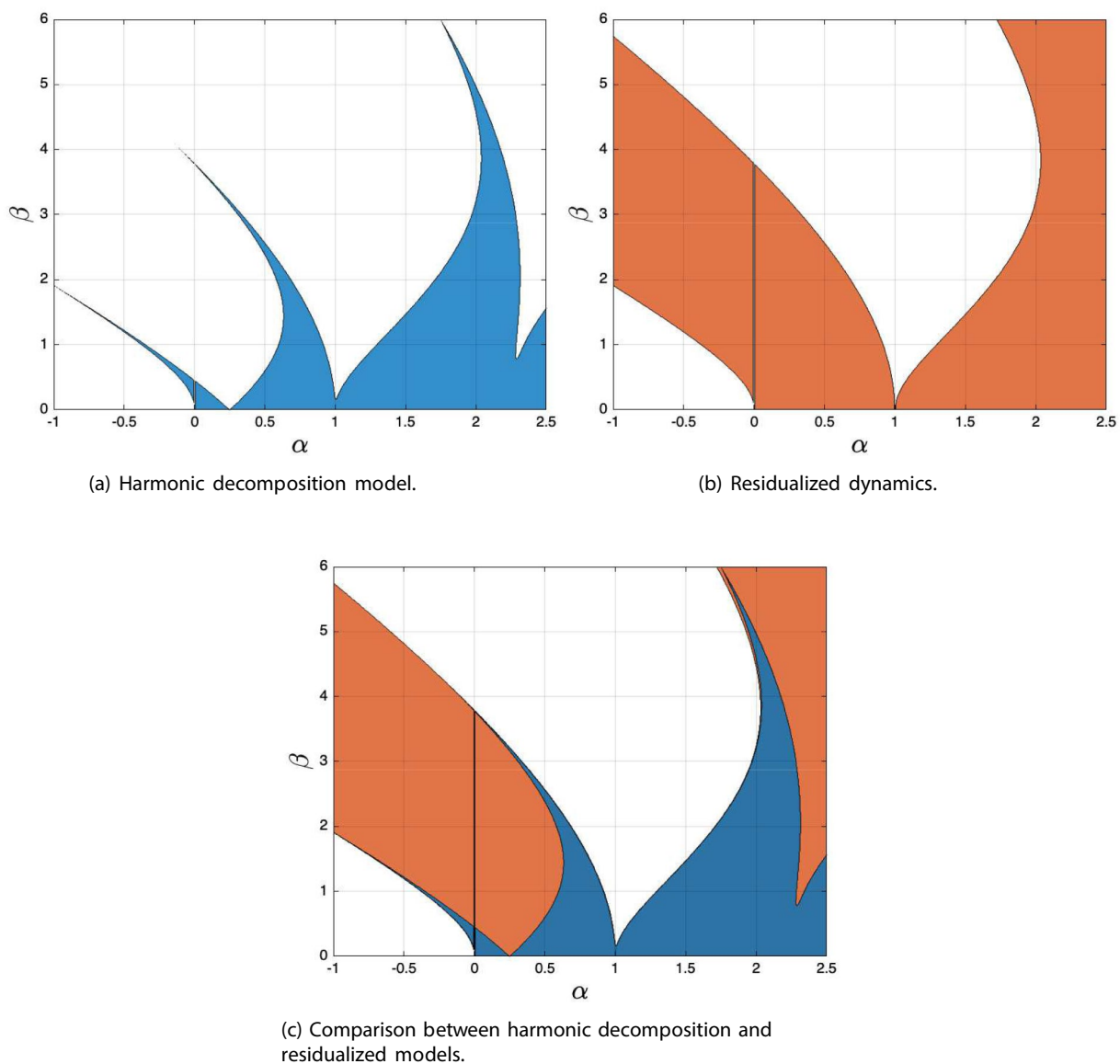
Fig. 4 Stability maps for varying α and β and a sinusoidal forcing function obtained by retaining up to the second state harmonic when performing harmonic decomposition (i.e., $N = 2$)
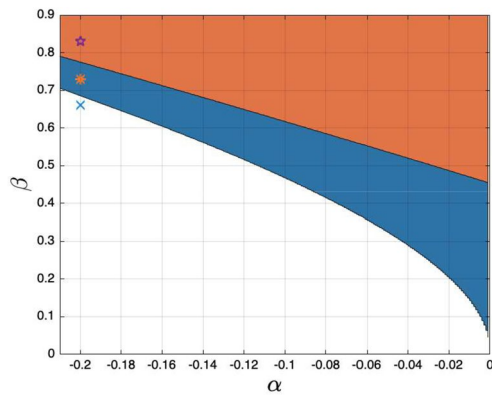
Fig. 5 Stability diagram for the undamped Mathieu equation. The markers indicate the cases for which time responses are calculated

harmonic decomposition model. Finally, Fig. 6c, which is representative of the case where $\alpha = -0.2$ and $\beta = 0.73$, shows unstable responses for Mathieu's equation and for the harmonic decomposition model, whereas the response of the residualized dynamics is stable. This can be explained by the fact that, for this particular combination of α and β, the stability map of the residualized dynamics predicts a stable behavior, whereas that obtained with the harmonic decomposition model predicts instability. This validates the stability map obtained with the harmonic decomposition model, while it confirms that the stability map obtained with the residualized dynamics only predicts the left boundaries of stability in the Ince-Strutt diagram.

(a) Case 1: $\alpha = -0.2$ and $\beta = 0.66$.

(b) Case 2: $\alpha = -0.2$ and $\beta = 0.73$.

(c) Case 3: $\alpha = -0.2$ and $\beta = 0.83$.

Fig. 6 Stability maps for varying α and β and a sinusoidal forcing function obtained by retaining up to the second state harmonic when performing harmonic decomposition (i.e., $N = 2$)

Fig. 7 Schematic of the closed-loop rotorcraft dynamics

Closed-Loop Dynamics
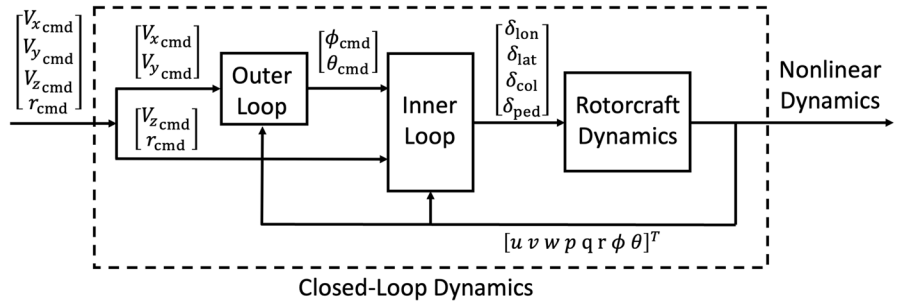
4 Simulation model

The nonlinear flight dynamics of a utility helicopter are modeled using PSUHeloSim [57], a MATLAB® implementation of the General Helicopter (GenHel) flight dynamics simulation model [58] with improved rotor, trimming, and linearization routines. PSUHeloSim is representative of a utility helicopter similar to a UH-60. Table 1 summarizes the salient characteristics of the UH-60-like simulation model. The model contains a 6-degree-of-freedom rigid-body dynamic model of the fuselage, nonlinear aerodynamic lookup tables for the fuselage, rotor blades, and empennage, rigid flap and lead-lag rotor blade dynamics, a three-state Pitt-Peters inflow model [59], and a Bailey tail rotor model [60]. The state vector is:

$$
\begin{aligned}
\boldsymbol{x}^T = \big[& u\,v\,w\,p\,q\,r\,\phi\,\theta\,\psi\,x\,y \\
& z\,\beta_0\,\beta_{0D}\,\beta_{1c}\,\beta_{1s}\,\dot{\beta}_0\,\dot{\beta}_{0D}\,\dot{\beta}_{1c}\,\dot{\beta}_{1s} \\
& \zeta_0\,\zeta_{0D}\,\zeta_{1c}\,\zeta_{1s}\,\dot{\zeta}_0\,\dot{\zeta}_{0D}\,\dot{\zeta}_{1c}\,\dot{\zeta}_{1s}\,\lambda_0\,\lambda_{1c}\,\lambda_{1s}\,\lambda_{0T} \big]
\end{aligned}
\tag{43}
$$

where:

  u, v, w are the longitudinal, lateral, and vertical velocities in the body-fixed frame,
  p, q, r are the roll, pitch, and yaw rates,
  ϕ, θ, ψ are the Euler angles,
  x, y, z are the positions in the North-East-Down (NED) frame,
  β_0, , β_{0D}, β_{1c}, β_{1s} are the flapping angles in multi-blade coordinates,
  ζ_0, ζ_{0D}, ζ_{1c}, ζ_{1s} are the lead-lag angles in multi-blade coordinates,
  λ_0, λ_{1c}, λ_{1s}, are the main rotor induced inflow ratio harmonics, and
  λ_{0T} is the tail rotor induced inflow ratio.

The state vector is conveniently partitioned into rigid-body and rotor states:

$$
\boldsymbol{x}_{\mathrm{RB}}^T = \big[u\,v\,w\,p\,q\,r\,\phi\,\theta\,\psi\,x\,y\,z \big]
\tag{44a}
$$

Table 1 General characteristics of the UH-60-like utility helicopter model

Parameter	Value	Units
Mass and inertia		
Gross weight, W	17, 000	lb
Roll-axis moment of inertia, I_{xx}	5000	sl-ft^2
Pitch-axis moment of inertia, I_{yy}	39,000	sl-ft^2
Yaw-axis moment of inertia, I_{zz}	39,000	sl-ft^2
Roll/yaw-axes product of inertia, I_{xz}	1900	sl-ft^2
Main rotor		
Number of blades, N_{b}	4	–
Radius, R	26.8	ft
Blade chord, c	1.73	ft
Blade twist, θ_{tw}	−13	deg
Flapping hinge offset	1.25	ft
Blade weight, W_{b}	256.9	lb
Blade first mass moment, M_β	86.7	sl-ft
Blade second mass moment, I_β	1512.6	sl-ft^2
Angular speed, Ω	27	rad/s
Tail Rotor		
Number of blades, $N_{\mathrm{b_{TR}}}$	4	–
Radius, R_{TR}	5.5	ft
Blade chord, c_{TR}	0.81	ft
Blade twist, $\theta_{\mathrm{tw_{TR}}}$	−17	deg
Blade second mass moment, $I_{\beta_{\mathrm{TR}}}$	3.10	sl-ft
Angular speed, Ω_{TR}	124.62	rad/s

$$
\begin{aligned}
\boldsymbol{x}_{\mathrm{R}}^T = \big[& \beta_0\,\beta_{0D}\,\beta_{1c}\,\beta_{1s}\,\dot{\beta}_0\,\dot{\beta}_{0D}\,\dot{\beta}_{1c}\,\dot{\beta}_{1s}\zeta_0 \\
& \zeta_{0D}\,\zeta_{1c}\,\zeta_{1s}\,\dot{\zeta}_0\,\dot{\zeta}_{0D}\,\dot{\zeta}_{1c}\,\dot{\zeta}_{1s}\,\lambda_0\,\lambda_{1c}\,\lambda_{1s}\,\lambda_{0T} \big]
\end{aligned}
\tag{44b}
$$

The control vector is:

$$
\boldsymbol{u}^T = \big[\delta_{\mathrm{lat}}\,\delta_{\mathrm{lon}}\,\delta_{\mathrm{col}}\,\delta_{\mathrm{ped}} \big]
\tag{45}
$$

where δ_{lat} and δ_{lon} are the main rotor lateral and longitudinal cyclic inputs, δ_{col} is the main rotor collective input, and δ_{ped} is the tail rotor collective, or pedal, input.

The bare-airframe dynamics are augmented with a multi-loop nonlinear dynamic inversion (NDI) control law largely based on [51, 53, 57, 61–66]. The schematics of the

closed-loop rotorcraft dynamics are shown in Fig. 7. The outer loop controller tracks longitudinal and lateral ground velocity commands in the heading frame and calculates the desired pitch and roll attitudes for the inner loop to track. The response type of the outer loop is Translational Rate Command (TRC). The inner loop achieves stability, disturbance rejection, and desired response characteristics about the roll, pitch, yaw, and heave axes. When coupled with the outer loop, an Attitude Command / Attitude Hold (ACAH) response is used for the roll and pitch axes, Rate Command / Attitude Hold (RCAH) is used for the yaw axis, and a TRC response is used for the heave axis.

5 Results

5.1 Vibrational stability due to blade imbalance

Consider an example involving the flight dynamics of a hovering helicopter experiencing rotor blade imbalance. Rotor blade imbalance might be caused by manufacturing imperfections in the blades, non-optimal rotor balancing, and/or rotor blade damage. Since helicopters are subjected to a variety of vibrations, it is feasible that vibrational effects might affect their stability characteristics. Traditionally, linear time invariant models of helicopter flight dynamics neglect vibrational effects, but through the use of harmonic decomposition [35] time periodic terms can be retained in the LTI models.

In general, the flight dynamics of this model are nonlinear time-periodic (NLTP), such that:

$$\dot{x} = f(x, u, \psi) \tag{46}$$

where $\psi = \Omega t$ is the azimuth angle of a reference main rotor blade. Blade imbalance is modeled by assuming one of the four rotor blades to have a different mass with respect to the others. The unbalanced blade mass is assumed to have values from 1 to 10% more than the others. While these values include some extreme cases (rotor imbalance in nominal conditions is not likely to exceed a few percents [67]) these could be feasible values in off-nominal conditions, i.e., when a blade is damaged. The reason 10% was selected for the maximum imbalance is that above this value, there was minimal change in the flight dynamics (as will be shown in the results below). Given this difference in mass, first and second flapping moments are varied assuming the same relative mass distribution as the nominal blade. Because blade imbalance results in a periodic forcing at one-per-rotor-revolution (1/rev), trim at hover will no longer be represented a single point in the state space but rather by a periodic orbit such that the trim state and control vectors are $x^*(\psi) = x^*(\psi + \Omega T)$ and $u^*(\psi) = u^*(\psi + \Omega T)$.

To solve for this periodic orbit, the modified harmonic balance algorithm of [47] is used. Figure 8 shows the periodic trim acceleration at the center of gravity (CG) over one rotor revolution. The rotor blade imbalance results in 1/rev vibrations with amplitudes of up to 0.5 g in the lateral and vertical acceleration for the 10% blade imbalance case. For reference, these vibrations are in line with those encountered by fixed-wing aircraft in severe turbulence [68–71].

Next, the flight dynamics are linearized about this periodic orbit to yield an LTP system. The LTP system is approximated with a higher-order LTI system by retaining up to the fifth harmonic of the fundamental frequency (i.e., the angular speed of the main rotor Ω) in the state vector (i.e., $N = 5$), up to the fourth harmonic in the output vector (i.e., $L = 4$), while retaining only the zeroth harmonic of the control input vector (i.e., $M = 0$). While the dominant oscillations at hover will be the 1/rev oscillations due to blade imbalance, small 4/rev oscillations may also be present, although these become significant only in forward flight. Thus, it is chosen to retain up to the fifth harmonic in the state vector [53] and up to the fourth harmonic in the outputs. Retaining only the zeroth harmonic in the control input relies on the assumption that no higher-harmonic control (HHC) is employed, which is typically the case for conventional rotorcraft.

The order of the higher-order LTI model is subsequently reduced to a 10-state model representative of the rigid-body dynamics and of the regressive flap mode. An 8-state model is also obtained, which is representative of the rigid-body dynamics only. Because this model does not retain the flapping states used to predict the regressive flap mode, its accuracy will be limited to frequencies up to approximately 4 rad/s. To validate the linearized models obtained via the
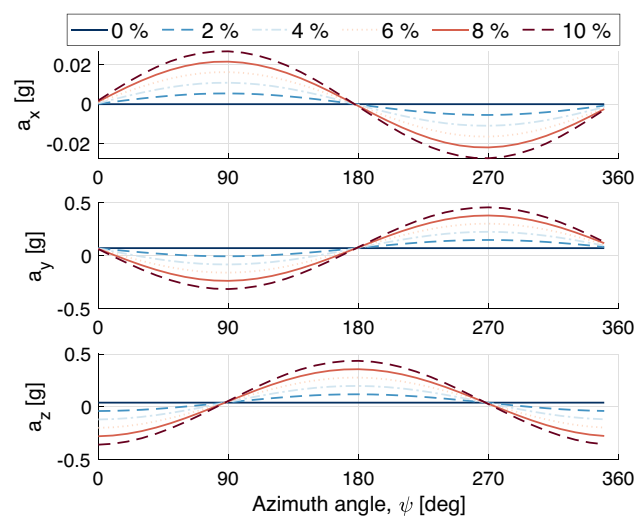
Fig. 8 Periodic trim acceleration at the CG over one rotor revolution for increasing blade imbalance

proposed method, the on-axis frequency responses of these models are compared to frequency responses extracted from frequency sweeps [72]. Because the dynamics of rotorcraft are unstable at hover, the control law described above is used to stabilize the hover dynamics during the frequency sweeps. The sweep inputs are injected between the inner loop and the rotorcraft dynamics. Because this is, in fact, a closed-loop identification problem where the inputs are highly-correlated, the method in [73] is used. Figure 9 shows the input/output data for a lateral stick input sweep with 0% blade imbalance case. More specifically, Fig. 9a shows the chirp inputs, Fig. 9b shows the total (or closed-loop) control inputs before the mixer, and Fig. 9c shows the angular rates sweep response.

Figure 10 shows the bare-airframe roll rate due to lateral input frequency responses for varying blade imbalance. Figure 10a corresponds to no blade imbalance, whereas

Fig. 10b corresponds to a 10% blade imbalance. These figures show that the frequency responses of high-order LTI model match those obtained from frequency sweeps for both cases, validating the LTI model. The 8-state model is shown to provide good accuracy up to about 4 rad/s, whereas the accuracy of the 10-state model extends up to about 10.5 rad/s. These results suggest that the linearization, harmonic decomposition, and successive model-order reduction are suitable for obtaining linearized models representative of rotor blade imbalance.

The effect of blade imbalance on the flight dynamics can be assessed via spectral analysis of the reduced-order system thus obtained. Figure 11 shows the eigenvalues of the 10-state model for blade imbalance varying from zero to 10%. Figure 11a shows all ten eigenvalues and the regressive flapping eigenvalues are clearly shown to migrate to the left of the complex plane for increasing imbalance, eventually
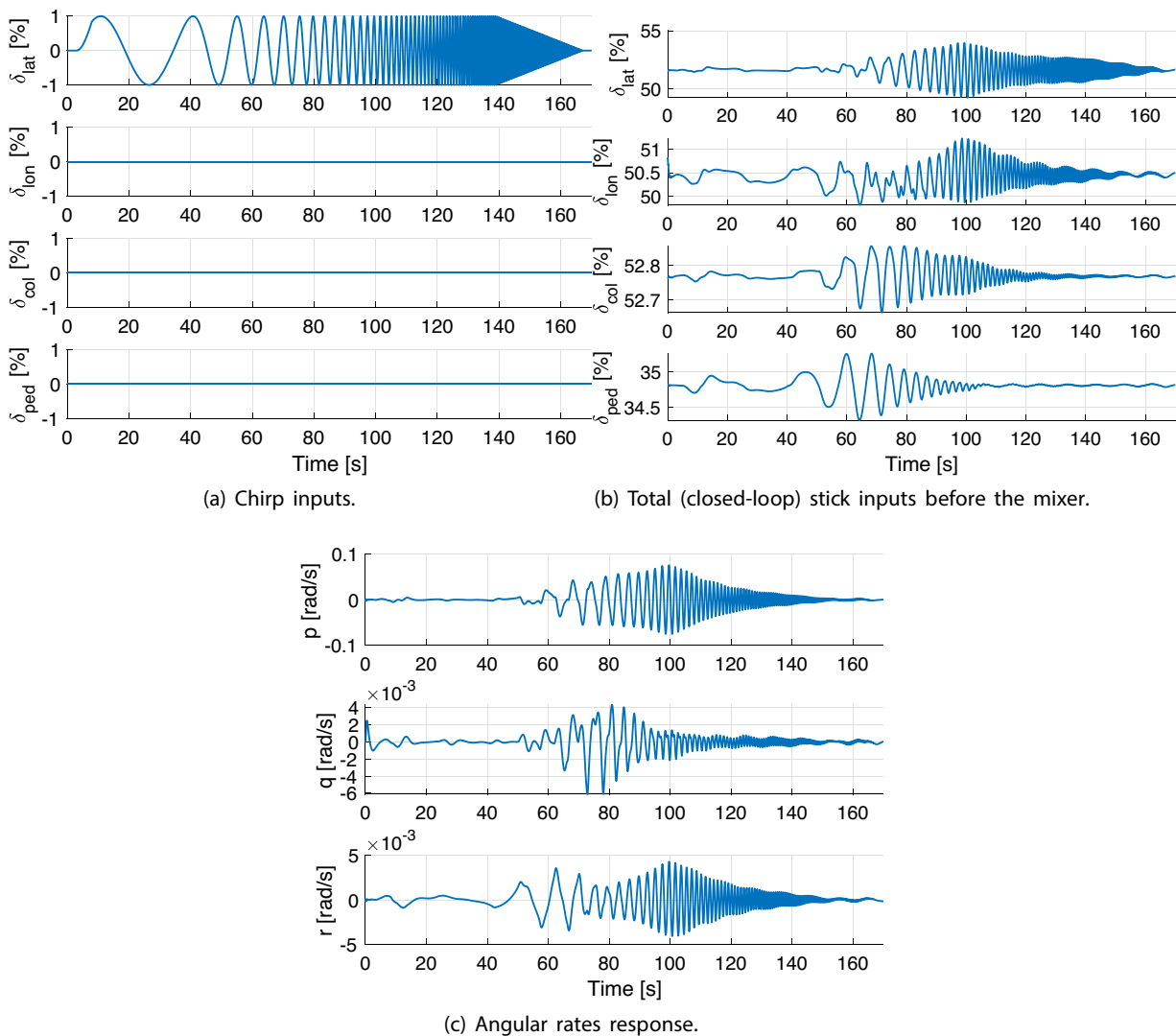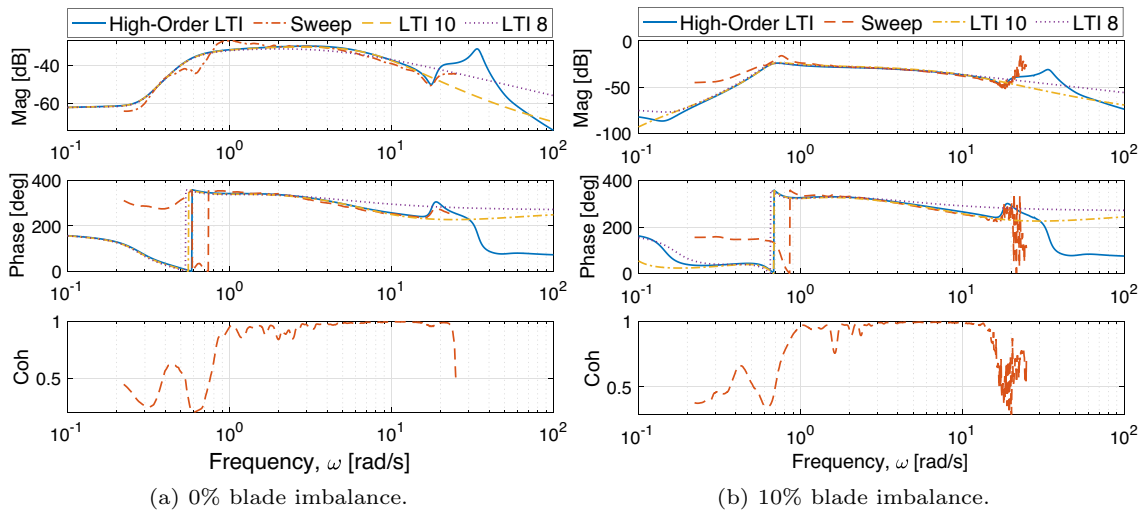

(a) Chirp inputs.

(b) Total (closed-loop) stick inputs before the mixer.

(c) Angular rates response.

Fig. 9 Example input/output data for a lateral stick sweep input

(a) 0% blade imbalance.

(b) 10% blade imbalance.

Fig. 10 Comparison between the roll rate due to lateral input frequency responses, $\frac{p}{\delta_{\text{lat}}}(s)$, obtained from linearized models and frequency sweeps

(a) Rigid-body and regressive flap dynamics.

(b) Rigid-body dynamics.
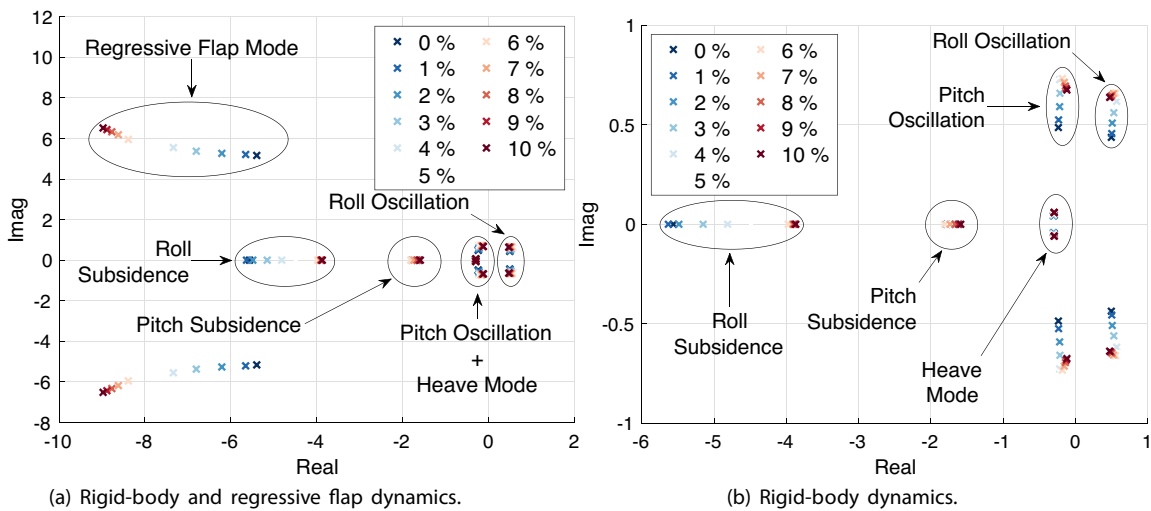
Fig. 11 Hover eigenvalues of the 10-state residualized model for varying blade imbalance
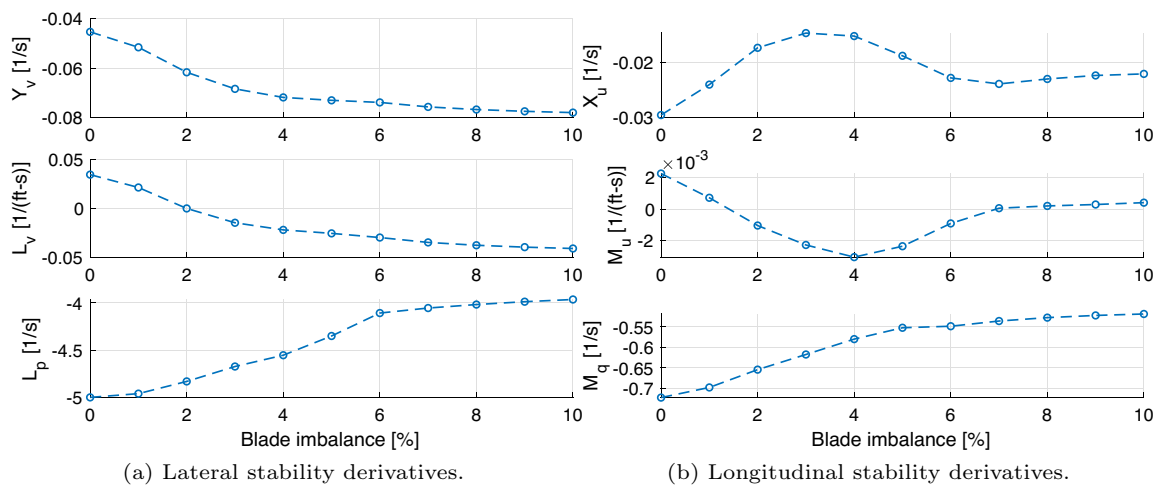
converging to fixed values as the imbalance approaches 10%. Figure 11b shows a detail of the rigid-body dynamics eigenvalues, where both the roll and pitch subsidence mode eigenvalues move toward the origin for increasing blade imbalance. This means that their frequency decreases with increasing blade imbalance. Moreover, both the roll and pitch oscillatory eigenvalues move away from the origin along the imaginary axis, which is indicative of higher frequency and lower damping. One difference, though, is that the pitch oscillatory eigenvalues move slightly to the right whereas the roll oscillatory eigenvalues move slightly to the left. The poles of the coupled yaw-heave mode are relatively unaffected compared to the other modes. These results are reported quantitatively in Table 2 for two cases: zero blade imbalance and 10% blade imbalance. Thus, it is concluded that rotor blade imbalance has a symmetric effect on the roll and pitch axes, in that it tends to decrease the frequency of the subsidence modes of the hovering cubic [4], while the oscillatory modes tend to increase in frequency and decrease in damping.

Figure 12 shows the lateral (Fig. 12a) and longitudinal (Fig. 12b) stability derivatives of the 8-state model for varying blade imbalance. The magnitude of the roll and pitch axes damping derivatives L_p and M_q is shown to decrease with increasing blade imbalance. On the other hand, while lateral speed stability (Y_v) becomes more negative with

Table 2 Hover modal characteristics for varying blade imbalance

Mode	Imbalance (%)	Eigenvalues (rad/s)	Natural frequency ω_n (rad/s)	Damping ratio, ζ
Roll subsidence	0	-5.56	–	1
	10	-3.93	–	1
Pitch subsidence	0	1.78	–	1
	10	1.57	–	1
Roll oscillation	0	$0.5 \pm 0.44i$	0.66	–
	10	$0.46 \pm 0.63i$	0.78	–
Pitch oscillation	0	$-0.23 \pm 0.49i$	0.54	0.44
	10	$0.11 \pm 0.66i$	0.67	0.17
Coupled Yaw-Heave	0	$-0.29 \pm 0.05i$	0.30	0.99
	10	$0.11 \pm 0.06i$	0.30	0.98

(a) Lateral stability derivatives.

(b) Longitudinal stability derivatives.

Fig. 12 Hover stability derivatives for varying blade imbalance

increasing blade imbalance, longitudinal speed stability (X_u) decreases in magnitude. It is notable that the roll and pitch moment derivatives due to lateral and longitudinal speed, L_v and M_u respectively, actually change signs for moderate amounts of imbalance (2%). These play a large part in the significant change in the frequency of oscillation modes associated with the hover cubic, as the frequency of these modes increased by more than 30% for a 2% blade imbalance.

In light of these results, the dynamics identified for a helicopter with an imbalanced rotor may indeed differ from those obtained from simulations where the rotor is perfectly balanced. A more in-depth explanation follows. When performing system/parametric identification from flight test data, which inevitably corresponds to some rotor imbalance on the real aircraft, what is identified are, in fact, dynamics equivalent to the residualized dynamics from the high-order LTI model. These can be referred to as the "true" dynamics. On the other hand, when performing flight dynamics

predictions from physics-based simulations, any periodic component in the flight dynamics due to blade imbalance is not modeled in that rotor blades are typically assumed as perfectly balanced. Even if blade imbalance was modeled, flight dynamics predictions adopting linearized models only typically consider the averaged (or zeroth harmonic) dynamics. This is equivalent to performing eigenanalysis on the averaged portion of the high-order LTI system in harmonic decomposition form. Or, in other terms, it corresponds to performing eigenanalysis on a reduced-order system obtained by truncating all of the higher-harmonic states from the high-order LTI system. Thus, any harmonic component is ignored. It is worth noting that the averaged dynamics of all cases presented with rotor imbalance is in fact the same. This concept is illustrated in Fig. 13, which features the frequency response of the zeroth harmonic of the roll rate to lateral inputs, i.e., $\frac{p_0}{\delta_{\text{lat}}}(s)$, for the high-order LTI model in harmonic decomposition form representative of a 10% rotor
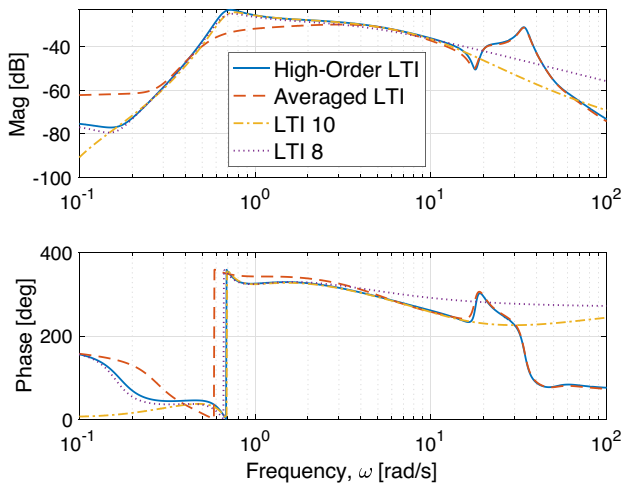
Fig. 13 Frequency response of the zeroth harmonic of the roll rate to lateral inputs, $\frac{p_0}{\delta_{\text{lat}}}(s)$

blade imbalance, the averaged dynamics, and the 8- and 10-state residualized models corresponding to a 10% rotor blade imbalance. The 8-state residualized model constitutes a good approximation of the high-order LTI up to approximately 4 rad/s. In fact, the 8-state model shows reduced phase roll-off after 4 rad/s. This is because it does not include the longitudinal and lateral flapping states needed to predict the regressive flap mode. The 10-state model is accurate up to approximately 10.5 rad/s. The average dynamics, however, fail to predict the response in low-to-mid frequencies of interest to flight dynamics (i.e., 0.3–30 rad/s). These differences will cause discrepancies in the estimation of the stability derivative L_p. The same concept applies to all other frequency responses of interest for the identification of reduced-order models of the rotorcraft flight dynamics.

## 5.2 Vibrational stability in high-speed forward flight

Consider now an example involving the flight dynamics of a helicopter in high-speed forward flight. In this condition, the asymmetry of lift between the advancing and retreating sides of the main rotor results in periodic forcing at number-of-blades-per-rotor-revolution (N_b/rev). As such, trim in high-speed forward flight will be represented by a periodic orbit with N_b/rev harmonics. For the helicopter in consideration, which features four main rotor blades, the periodic orbit will be dominated by 4/rev harmonics. To solve for this periodic orbit, the same harmonic balance algorithm of the previous example [47] is used. The flight condition chosen is 140 kts forward flight. Figure 14 shows the periodic trim acceleration at the center of gravity (CG) over one rotor revolution.
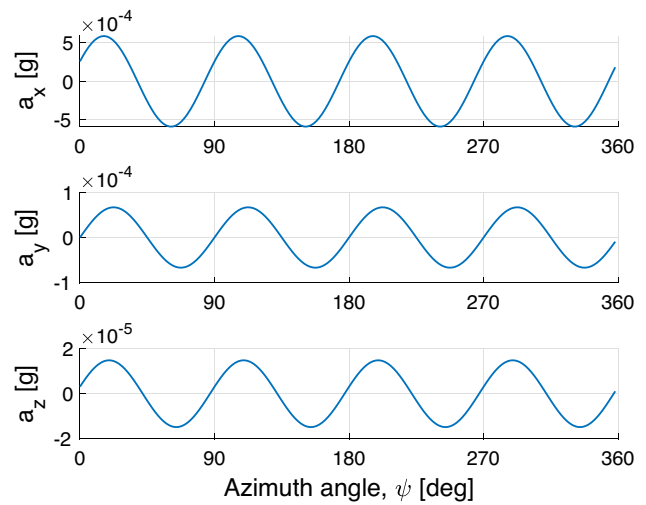
Fig. 14 Periodic trim acceleration at the CG over one rotor revolution for a 190 kts forward flight condition

This figure clearly shows the 4/rev vibrations. It is worth noting that while dynamic stall effects are likely prevalent in this flight condition due, the simulation model employed in this study does incorporate dynamic stall models. As such, the vibratory load predictions are likely to be conservative.

Like before, the flight dynamics are linearized about this periodic orbit to yield an LTP system. The LTP system is approximated with a higher-order LTI system by retaining up to the fifth harmonic of the fundamental frequency. The effect of vibrations due to N_b/rev rotor loads on the flight dynamics can be assessed by comparing the eigenvalues of the high-order LTI model with those of the averaged dynamics. Figure 15 shows the rigid-body eigenvalues of said models. Clearly, a mismatch exists between the coupled pitch/roll
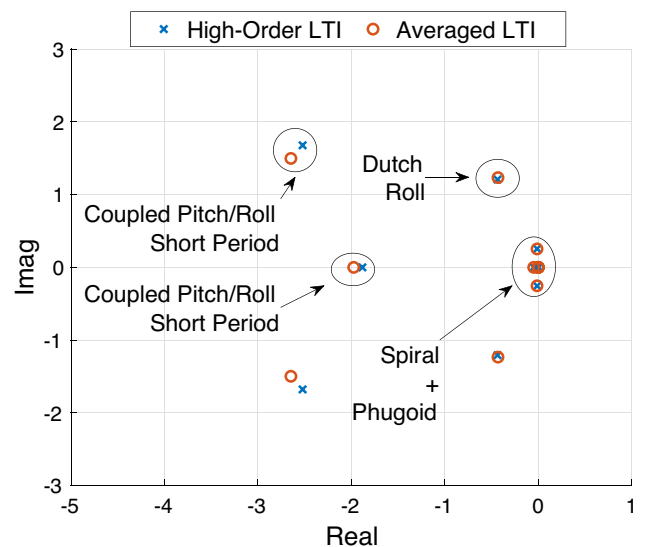
Fig. 15 Rigid-body eigenvalues for a 140 kts forward flight condition

Table 3 Modal characteristics at 140 kts forward flight

Mode	Model	Eigenvalues (rad/s)	Natural frequency, ω_n (rad/s)	Damping ratio, ζ
Spiral	High-order LTI	-0.05	–	1
	Averaged LTI	-0.05	–	1
Phugoid	High-order LTI	$-0.01 \pm 0.25i$	0.25	0.04
	Averaged LTI	$-0.01 \pm 0.25i$	0.25	0.04
Dutch roll	High-order LTI	$-0.44 \pm 1.21i$	1.29	0.34
	Averaged LTI	$-0.43 \pm 1.23i$	1.3	0.33
Coupled roll/pitch	High-order LTI	-1.88	–	1
Short period	Averaged LTI	-1.97	–	1
Coupled roll/pitch	High-order LTI	$-2.52 \pm 1.68i$	3.03	0.83
Short period	Averaged LTI	$-2.65 \pm 1.49i$	3.04	0.87

short period eigenvalues of the two models in that the averaged dynamics over-predicts the damping of the short-period mode. The other modes largely remain unaffected. These results are reported quantitatively in Table 3. It is concluded that N_b/rev rotor loads in high-speed forward flight affect the coupled roll/pitch short period in a way that reduces the damping of the mode. Failing to account for the N_b/rev harmonics in the linearized dynamics may lead to over-prediction of the coupled roll/pitch short period damping.

6 Conclusion

This article investigated vibrational stabilization effects in rotorcraft flight dynamics. Starting from a simple example involving an inverted pendulum, the use of the harmonic decomposition method for the study of vibrational stabilization effects was extended to rotorcraft applications. The methodology was used to analyze the effect of blade imbalance at hover and N_b/rev loads in high-speed forward flight on the flight dynamics of a helicopter. Based on this work, the following conclusions can be reached:

1. The vibrations induced by rotor blade imbalance did not stabilize the hovering dynamics of a hovering helicopter, but these vibrations had a significant effect on the hovering dynamics for blade imbalances as small as 2%. Increasing rotor blade imbalance results in a symmetric effect on the roll and pitch axes, in that it tends to decrease the frequency of the subsidence modes of the hovering cubic, while the unstable oscillatory modes tend to increase in frequency and decrease in damping. The yaw/heave dynamics are relatively unaffected compared to the lateral and longitudinal axes.

2. Rotor blade imbalance of 2% or more resulted in a change of sign in the roll and pitch moment due to speed derivatives near hover (L_v and M_u respectively). These derivatives have a significant impact on the oscillation associated with the hover cubic, and indeed significant changes in the frequencies of these modes were observed for 2% blade imbalance.

3. Although past research refers to vibrational "stabilization" to describe the effect of periodic forcing on system stability, the results indicate that for helicopters with imbalanced blades, many of vibrational effects are actually destabilizing, resulting in lower frequency (larger time constants) for the roll and pitch subsidence modes and lower damping ratio for the hover oscillations.

4. N_b/rev rotor loads in high-speed forward flight affect the coupled roll/pitch short period in a way that reduces the damping of the mode. Failing to account for the N_b/rev harmonics in the linearized dynamics may lead to over-prediction of the coupled roll/pitch short period mode damping.

Declarations

References

1. Meerkov, S.: Principle of vibrational control: theory and applications. IEEE Trans. Autom. Control **25**(4), 755–762 (1980). https://doi.org/10.1109/TAC.1980.1102426
2. Bellman, R., Bentsman, J., Meerkov, S.: Vibrational control of nonlinear systems: vibrational stabilizability. IEEE Trans. Autom. Control **31**(8), 710–716 (1986). https://doi.org/10.1109/TAC.1986.1104384
3. Levi, M., Weckesser, W.: Stabilization of the inverted linearized pendulum by high frequency vibrations. SIAM Rev. **37**(2), 219–223 (1995). https://doi.org/10.1137/1037044
4. McRuer, D.T., Ashkenas, I.L., Graham, D.: 6. Aircraft Dynamics and Automatic Control. Princeton University Press, Princeton (1973)
5. Taha, H.E., Tahmasian, S., Woosley, C.A., Nafayeh, A.H., Hajj, M.R.: The need for higher-order averaging in the stability analysis of hovering, flapping-wing flight. Bioinspir. Biomim. **10**(1), 1–15 (2015). https://doi.org/10.1088/1748-3190/10/1/016002
6. Taha, H.E., Kiani, M., Hendrick, T.L., Greeter, J.S.M.: Vibrational control: a hidden stabilization mechanism in insect flight. Sci. Robot. (2020). https://doi.org/10.1126/scirobotics.abb1502
7. Saetti, U., Horn, J.F., Berger, T., Lopez, M.J.S., Tischler, M.B.: Identification of linear time-periodic systems from rotorcraft flight test data. J. Guid. Control Dyn. **42**(10), 2288–2296 (2019). https://doi.org/10.2514/1.G004406
8. Hayajnh, M.A., Saetti, U., Pradad, J.V.R.: Identification of high-order linear time-invariant models from periodic nonlinear system responses. In: Proceedings of the VFS Aeromechanics for Advanced Vertical Flight Technical Meeting, San Jose, CA (2022)
9. Saetti, U., Rogers, J.D.: Harmonic decomposition models of flapping-wing flight for stability analysis and control design. J. Guid. Control Dyn. (2022). https://doi.org/10.2514/1.G006447
10. Lopez, M.J.S., Prasad, J.V.R.: Estimation of modal participation factors of linear time periodic systems using linear time invariant approximations. J. Am. Helicopter Soc. **61**(4), 1–4 (2016). https://doi.org/10.4050/JAHS.61.045001
11. Maggia, M., Eisa, S.A., Taha, H.E.: On higher-order averaging of time-periodic systems: reconciliation of two averaging techniques. Nonlinear Dyn. **99**, 813–836 (2020). https://doi.org/10.1007/s11071-019-05085-4
12. Tamer, A.: Generalized aeroservoelastic stability analysis of rotorcraft. PhD thesis, Politecnico di Milano, Milano, Italy (2015)
13. Floquet, G.: Sur les équations différentielles linéaires à coefficients périodiques. Annales scientifiques de l'École Normale Supérieure **2**(12), 47–88 (1883). https://doi.org/10.24033/asens.220
14. Dietl, J.M., Garcia, E.: Stability in ornithopter longitudinal flight dynamics. J. Guid. Control Dyn. **31**(4), 1152–1157 (2008). https://doi.org/10.2514/1.33561
15. Bierling, T., Patil, M.: Stability and power optimality in time-periodic flapping wing structures. J. Fluids Struct. **38**, 238–254 (2013). https://doi.org/10.1016/j.jfluidstructs.2012.12.006
16. Su, W., Cesnik, C.E.S.: Flight dynamic stability of a flapping wing micro air vehicle in hover. In: AIAA Paper 2011–2009, Proceedings of the 52nd AIAA/ASME/ASCE/AHS/ACS Structures, Structural Dynamics, and Materials Conference, Denver, CO (2011). https://doi.org/10.2514/6.2011-2009
17. Bolender, M.A.: Open-loop stability of flapping flight in hover. In: AIAA Paper 2010-7552, AIAA Guidance, Navigation, and Control Conference, Toronto, Ontario, Canada (2010). https://doi.org/10.2514/6.2010-7552
18. Sanders, V.F.J.A., Murdock, J.: Averaging: The Periodic Case. Averaging Methods in Nonlinear Dynamical Systems. Springer, Princeton (2007). https://doi.org/10.1007/978-0-387-48918-6
19. Hassan, A.M., Taha, H.E.: Higher-order averaging analysis of the nonlinear time-periodic dynamics of hovering insects/flapping-wing micro-air-vehicles. In: Proceedings of the 55th Conference on Decision and Control, Las Vegas, NV (2016). https://doi.org/10.1109/CDC.2016.7799424
20. Oppenheimer, M.W., Weintraub, I.E., Sighorsson, Doman, D.B.: Quarter cycle modulation of a minimally actuated biomimetic vehicle. In: AIAA Paper 2014-1467, AIAA SciTech Forum, National Harbor, MD (2014). https://doi.org/10.2514/1.G000548
21. Oppenheimer, M.W., Weintraub, I.E., Sighorsson, D.D.B.: Control of a minimally actuated biometric vehicle using quarter-cycle wingbeat modulation. J. Guid. Control Dyn. **38**(7), 1187–1196 (2015). https://doi.org/10.2514/1.G000548
22. Sigthorsson, D.O., Oppenheimer, M.W., Doman, D.B.: Flapping-wing micro-air-vehicle control employing triangular waves strokes and cycle averaging. In: AIAA Paper 2010-7553, AIAA Guidance, Navigation, and Control Conference, Toronto, Ontario, Canada (2010). https://doi.org/10.2514/6.2010-7553
23. Sigthorsson, D.O., Oppenheimer, M.W., Doman, D.B.: Flapping-wing micro-air-vehicle 4-dof controller applied to a 6-dof model. In: AIAA Paper 2010-7554, AIAA Guidance, Navigation, and Control Conference, Toronto, Ontario, Canada (2010). https://doi.org/10.2514/6.2010-7554
24. Finio, B.M., Perez-Arancibia, N.O., Wood, R.J.: System identification and linear time-invariant modeling of an insect-sized flapping-wing micro air vehicle. In: 2011 IEEE/ESJ International Conference on Intelligent Robots and Systems, San Francisco, CA (2011). https://doi.org/10.1109/IROS.2011.6094421
25. Cheng, D., Deng, X.: Translational and rotational damping of flapping flight and its dynamics and stability at hovering. IEEE Trans. Robot. **27**(5), 849–864 (2011). https://doi.org/10.1109/TRO.2011.2156170
26. Vela, P.A.: Averaging and control of nonlinear systems (with application to biomimetic locomotion). PhD thesis, California Institute of Technology, Pasadena, CA (2003)
27. Tamer, A., Masarati, P.: Stability of nonlinear, time-dependent rotorcraft systems using lyapunov characteristic exponents. J. Am. Helicopter Soc. **61**(2), 1–1212 (2016). https://doi.org/10.4050/JAHS.61.022003
28. Tamer, A., Masarati, P.: Sensitivity of lyapunov exponents in design optimization of nonlinear dampers. J. Comput. Nonlinear Dyn. (2019). https://doi.org/10.1115/1.4041827
29. Tamer, A., Masarati, P.: Generalized quantitative stability analysis of time-dependent comprehensive rotorcraft systems. Aerospace (2022). https://doi.org/10.3390/aerospace9010010
30. Tamer, A., Masarati, P.: Quantitative aeroelastic stability prediction of wings exhibiting nonlinear restoring forces. J. Math. Sci. Model. **6**(2), 76–86 (2023). https://doi.org/10.33187/jmsm.1214586
31. Cassoni, G., Zanoni, A., Tamer, A., Masarati, P.: Stability of rotorcraft ground resonance by estimating lyapunov characteristic exponents from multibody dynamics. In: Proceedings of the 18th International Conference on Multibody Systems, Nonlinear Dynamics, and Control (MSNDC), St. Louis, MO (2022). https://doi.org/10.1115/DETC2022-88995
32. Cassoni, G., Cocco, A., Tamer, A., Zanoni, A., Masarati, P.: Tiltrotor whirl-flutter stability investigation using lyapunov characteristic exponents and multibody dynamics. In: Proceedings of the 48th European Rotorcraft Forum, Winterthur, Switzerland (2022). https://doi.org/10.1115/DETC2022-88995
33. Pandyan, R., Sinha, S.C.: Time-varying controller synthesis for nonlinear systems subjected to periodic parametric loading. J. Vib. Control **7**(1), 73–90 (2001). https://doi.org/10.1177/107754630100700105

34. Colaneri, P., Celi, R., Bittanti, S.: Constant coefficient representation of discrete periodic linear systems. In: Proceedings of the 4th Decennial Specialists' Conference on Aeromechanics, San Francisco, CA (2004)

35. Lopez, M.J.S., Prasad, J.V.R.: Linear time invariant approximations of linear time periodic systems. J. Am. Helicopter Soc. **62**(1), 1–10 (2017). https://doi.org/10.4050/jahs.62.012006

36. Lopez, M.J.S.: Linear time invariant approximations of linear time periodic systems for integrated flight and vibration control. PhD thesis, Georgia Institute of Technology, Atlanta, GA (2016)

37. Saetti, U., Horn, J.F.: Linear time-invariant approximations of nonlinear time-periodic systems. J. Am. Helicopter Soc. **68**(1), 1–10 (2023). https://doi.org/10.4050/JAHS.68.012006

38. Prasad, J.V.R., Olcer, F.E., Sankar, L.N., He, C.: Linear time invariant models for integrated flight and rotor control. In: Proceedings of the 35 European Rotorcraft Forum, Hamburg, Germany (2009)

39. Lopez, M., Prasad, J.V.R., Tischler, M.B., Takahashi, M.D., Cheung, K.K.: Simulating HHC/AFCS interaction and optimized controllers using piloted maneuvers. In: Proceedings of the 71st Annual Forum of the American Helicopter Society, Virginia Beach, VA (2015)

40. Padthe, A.K., Friedmann, P.P., Lopez, M., Prasad, J.V.R.: Analysis of high fidelity reduced-order linearized time-invariant helicopter models for integrated flight and on-blade control applications. In: Proceedings of the 41st European Rotorcraft Forum, Munich, Germany (2015)

41. Saetti, U., Horn, J.F.: Load alleviation flight control design using high-order dynamic models. J. Am. Helicopter Soc. (2020). https://doi.org/10.4050/JAHS.65.032009

42. Saetti, U., Horn, J.F., Berger, T., Tischler, M.B.: Handling-qualities perspective on rotorcraft load alleviation control. J. Guid. Control Dyn. (2020). https://doi.org/10.2514/1.G004965

43. Scaramal, M., Horn, J.F., Saetti, U.: Load alleviation control using dynamic inversion with direct load feedback. In: Proceedings of the 77th Annual Forum of the Vertical Flight Society, Virtual (2021)

44. Mballo, C.E., Prasad, J.V.R.: A real time scheme for rotating system component load estimation using fixed system measurements. In: Proceedings of the 74th Annual Forum of the Vertical Flight Society, Phoenix, AZ (2018)

45. Mballo, C.E., Prasad, J.V.R.: Real time rotor component load limiting via model predictive control. In: Proceedings of the 75th Annual Forum of the Vertical Flight Society, Philadelphia, PA (2019)

46. Saetti, U., Lovera, M.: Time-periodic and high-order time-invariant linearized models of rotorcraft: a survey. J. Am. Helicopter Soc. (2022). https://doi.org/10.4050/JAHS.67.012008

47. Saetti, U., Rogers, J.D.: Revisited harmonic balance trim solution method for periodically-forced flight vehicles. J. Guid. Control Dyn. **44**(5), 1008–1017 (2021). https://doi.org/10.2514/1.G005553

48. Kokotovic, P.V., O'Malley, R.E., Sannuti, P.: Singular perturbations and order reduction in control theory, an overview. Automatica **12**(2), 123–132 (1976). https://doi.org/10.1016/0005-1098(76)90076-5

49. Frazzoli, E., Dahleh, M.A., Feron, E.: Maneuver-based motion planning for nonlinear systems with symmetries. IEEE Trans. Robot. **21**(6), 1077–1091 (2005). https://doi.org/10.1109/TRO.2005.852260

50. Saetti, U., Horn, J.F., Brentner, K.S.: Linearized models of the coupled rotorcraft flight dynamics and acoustics for real-time noise prediction. J. Am. Helicopter Soc. (2024). https://doi.org/10.4050/JAHS.69.022002

51. Saetti, U., Bugday, B.: Tiltrotor simulations with coupled flight dynamics, state-space aeromechanics, and aeroacoustics. J. Am. Helicopter Soc. (2024). https://doi.org/10.4050/JAHS.69.012003

52. Saetti, U., Horn, J.F.: Load alleviation control design using harmonic decomposition models, rotor state feedback, and redundant control effectors. In: American Helicopter Society 74th Annual Forum Proceedings, Phoenix, AZ (2018)

53. Saetti, U.: Rotorcraft flight control design with alleviation of unsteady rotor loads. PhD thesis, Pennsylvania State University, University Park, PA (2019). https://doi.org/10.13140/RG.2.1.2259.3529

54. Berg, M.J., Wickramasinghe, I.P.M.: Vibrational control without averaging. Automatica **58**, 72–81 (2015). https://doi.org/10.1016/j.automatica.2015.04.028

55. Berg, J., Wickramasinghe, I.P.M.: Vibrational control of Mathieu's equation. In: Proceedings of the IEEE/ASME International Conference on Advanced Intelligent Mechatronics (2013). https://doi.org/10.1109/AIM.2013.6584172

56. Kapitza, P.L.: Dynamic stability of the pendulum with vibrating suspension point (1951). Collected Papers of P. L. Kapitza, vol. 2, pp. 714–726 (1965). https://doi.org/10.4050/jahs.62.012006

57. Horn, J.F.: Non-linear dynamic inversion control design for rotorcraft. Aerospace (2019). https://doi.org/10.3390/aerospace6030038

58. Howlett, J.J.: Uh-60a black hawk engineering simulation program. volume 1: mathematical model. Technical report (NASA-CR-166309, 1980)

59. Pitt, D.M., Peters, D.A.: Theoretical prediction of dynamic-inflow derivatives. In: Proceedings of the 6th European Rotorcraft and Powered Lift Aircraft Forum, Bristol, England (1980)

60. Bailey, F.J.: A simplified theoretical model of determining the characteristics of a lifting rotor in forward flight. Technical report (NACA Report No. 716, 1941)

61. Saetti, U., Horn, J.F., Lakhmani, S., Lagoa, C., Berger, T.: Design of dynamic inversion and explicit model following control laws for quadrotor uas. J. Am. Helicopter Soc. **65**(3), 1–1616 (2020). https://doi.org/10.4050/JAHS.65.032006

62. Saetti, E.J.U., Horn, J.F.: Flight dynamics and control of an evtol concept aircraft with a propeller-driven rotor. J. Am. Helicopter Soc. **67**(3), 153–166 (2022). https://doi.org/10.4050/JAHS.67.032012

63. Saetti, U., Rogers, J.D.: Dynamic inversion-based flare control law for autonomous helicopter autorotation. In: AIAA Paper 2022-1645, Proceedings of AIAA SciTech Forum (2022). https://doi.org/10.2514/6.2022-1645

64. Saetti, U., Horn, J.F.: Flight simulation and control using the Julia language. In: Proceedings of the AIAA SciTech Forum (2022). https://doi.org/10.2514/6.2022-2354

65. Saetti, U., Bugday, B.: Tiltrotor simulations with coupled flight dynamics, state-space aeromechanics, and aeroacoustics. J. Am. Helicopter Soc. **69**(1), 1–1616 (2024). https://doi.org/10.4050/JAHS.69.012003

66. Saetti, U., Rogers, J.D., Alam, M., Jump, M.: Tau theory-based flare control in autonomous helicopter autorotation. Aerospace (2024). https://doi.org/10.3390/aerospace11010033

67. Wang, J., Chopra, I.: Dynamics of helicopters in ground resonance with and without blade dissimilarities. In: Proceedings of the AIAA Dynamics Specialists Conference (1992). https://doi.org/10.2514/6.1992-2108

68. Chan, S.T., Mok, C.W.: Comparison of doppler lidar observations of severe turbulence and aircraft data. In: American Metereological Society 11th Conference on Aviation, Range, and Aerospace Metereology, Hyannis, MA (2014)

69. Koch, S.E., Jamison, B.D., Lu, C., Smith, T.L., Tollerud, E.I., Girz, C., Wang, N., Lane, T.P., Shapiro, M.A., Parrish, D.D., Cooper, O.R.: Turbulence and gravity waves within an

upper-level front. J. Atmos. Sci. **62**(11), 3885–3908 (2005). https://doi.org/10.1175/JAS3574.1

70. Crouse, G.L.: Design for passenger comfort and all weather operation. In: 7th AIAA ATIO Conference, 2nd CEIAT International Conference on Innovation and Integration in Aero Sciences, 17th LTA Systems Technology Conference; Followed by 2nd TEOS Forum, Belfast, Northern Ireland (2014). https://doi.org/10.2514/6.2007-7861

71. Lee, D.B., Chun, H.Y.: A numerical study of aviation turbulence encountered on 13 February 2013 over the yellow sea between china and Korea. J. Appl. Meteorol. Climatol. **57**(4), 1043–1060 (2018). https://doi.org/10.1175/JAMC-D-17-0247.1

72. Tischler, M.B., Remple, R.K.: Aircraft and Rotorcraft System Identification, 2nd edn. American Institute of Aeronautics and Astronautics (2012) **(Chap. 5, 13, 17)**. https://doi.org/10.2514/4.868207

73. Berger, T., Tischler, M.B., Knapp, M.E., Lopez, M.J.S.: Identification of multi-input systems in the presence of highly correlated inputs. J. Guid. Control Dyn. **41**(10), 2247–2257 (2018). https://doi.org/10.2514/1.G003530